

Correlator delay models and katpoint

Ludwig Schwardt
SARAO

29 May 2020

Abstract

Compare the correlator delay model of katpoint to the one in CALC and determine whether it can be improved (also including atmospheric effects). Katpoint will be based on the Astropy library in the near future, and this serves as a comparison.

1 Introduction

A fundamental quantity in radio interferometry is the difference in the arrival time of a coherent wavefront at the various receptors that constitute the interferometric array. Estimates of these delays enable the received signals to be aligned in time before correlation, which improves correlator efficiency (or allows any correlation in the first place).

The total delay can be divided into three components: geometric delay, electronic or cable delay, and atmospheric delay.

The **geometric** delay is the most important component, involving all effects governed by the location of each receptor on Earth, the position and velocity of the Earth and other Solar System objects, the orientation of the Earth and how it wobbles, as well as shifts in the Earth's crust and antenna axis offsets. The Earth orientation also includes the effects of the chosen time scale.

If the receptor has a steerable dish on an azimuth-elevation mount, as in the case of the MeerKAT telescope, its location (or phase reference point) is defined as the point on the azimuth axis that is closest to the elevation axis.

The **electronic or cable delay** is a fixed delay per receptor input representing the difference between the time that a wavefront passes through the receptor phase reference point, and the timestamp associated with its occurrence in the sampled time series of that input. This delay component will not be considered in this report.

The **atmospheric delay** is due to propagation of the wavefront through the layers of the atmosphere, especially the neutral troposphere (and stratosphere) and the ionised ionosphere. It is the extra time

$$\Delta t = \frac{1}{c} \int (n(x) - 1) dx \quad (1)$$

taken by the wavefront to travel through a medium with refractive index n with a phase velocity of c/n along the x direction, compared with the time it would have taken travelling with the velocity of light, c , in a vacuum. This ignores refractive bending of the ray which increases the path length very slightly. The atmospheric delay is conveniently expressed as an equivalent excess path length

$$L = c\Delta t = 10^{-6} \int N(x) dx \quad (2)$$

in terms of the radio refractivity

$$N = 10^6(n - 1) \text{ [ppm]}, \quad (3)$$

which is the deviation of the refractive index from unity expressed in parts per million. This report only considers systematic atmospheric refraction with straightforward corrections and ignores irregular refraction caused by e.g. approaching weather systems, travelling disturbances and diurnal gradients. A discussion of the relative importance of these effects for interferometers can be found in [1, 2].

1.1 Tropospheric delay

The “tropospheric” delay also includes contributions from neutral gases above the troposphere, like the stratosphere. The radio refractivity is predicted by an atmospheric model¹. We determine the excess path length in the zenith direction L_0 (or zenith delay) at each receptor by evaluating Eq. (2). The atmospheric delay then increases monotonically with zenith angle² due to the increasing air mass between the source and the receptor. This dependence is typically modelled separately.

1.1.1 Excess path length in the zenith direction

The density of various gases in the atmosphere decreases approximately exponentially with height above the Earth’s surface, which allows the integral in Eq. (2) to be approximated as

$$L_0 \approx 10^{-6} N_0 h_0, \quad (4)$$

where N_0 is the surface refractivity and h_0 is the scale height, the parameter of the exponential distribution that serves as the effective thickness of the relevant atmospheric layer.

The simple R uger refractivity model [4] is accurate to 1% below 100 GHz. It allows the tropospheric zenith delay to be split into a “dry” and “wet” component³. To first order, the dry component only depends on atmospheric pressure, while the wet component depends on temperature and relative humidity via the partial pressure of water vapour.

¹This follows the derivation in Chapter 13 of [2], referencing equations (13.4), (13.5), (13.6), (13.13), (13.15), (13.17b), (13.38), (13.40) and (13.41), as well as parts of [3].

²Recall that zenith angle is related to the elevation angle e in degrees by $z = 90^\circ - e$.

³The “dry” component also includes a small contribution due to the induced dipole moment of water vapour and is better described as the hydrostatic component [5], while the “wet” component describes the contribution due to the permanent dipole moment of water vapour.

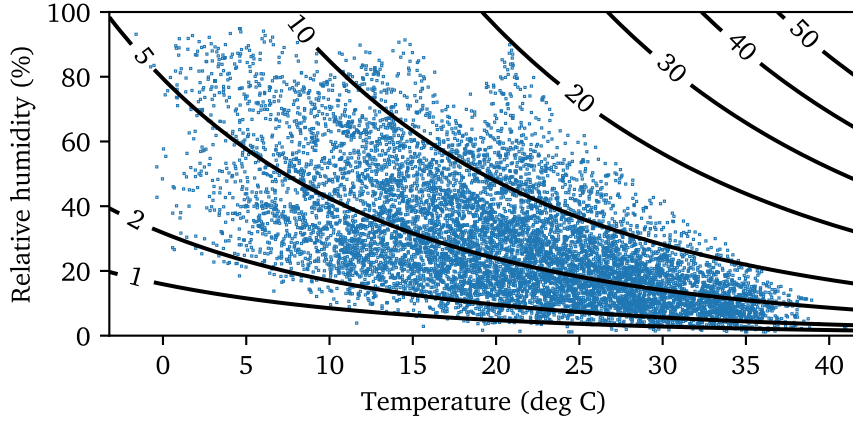


Figure 1: The excess path length (in cm) due to water vapour in the zenith direction at the MeerKAT site during 2019.

The dry excess path length in the zenith direction is

$$L_{0d} \approx 2.28 \times 10^{-3} P \text{ [m]} \quad (5)$$

for an atmosphere in hydrostatic equilibrium with the temperature, mixing ratio and gravitational acceleration all constant with height, a scale height of about 8 km and an atmospheric pressure of P hPa at the surface. The MeerKAT site has $L_{0d} \approx 205 \pm 3$ cm given its typical atmospheric pressure range of 901 ± 15 hPa.

The distribution of water vapour in the atmosphere is harder to model but is also approximately exponential on average, with a lower scale height of 2 km. This simple model results in a wet excess path length in the zenith direction of

$$L_{0w} \approx 760 \frac{P_w}{T^2} \text{ [m]}, \quad (6)$$

where P_w is the partial pressure of water vapour in hPa and T is the temperature in K (both at the Earth's surface). The partial pressure P_w is obtained from the relative humidity P_w/P_{ws} and the partial pressure of water vapour for saturated air, estimated to within 1% by Crane's formula [6] as

$$P_{ws} = 6.11 \left(\frac{T}{273} \right)^{-5.3} \exp \left(25.2 \frac{T-273}{T} \right) \text{ [hPa]}. \quad (7)$$

The MeerKAT site has a median zenith wet excess path length $L_{0w} \approx 5$ cm, which corresponds to an average temperature of 21°C and relative humidity of 23%, but it can range from 0.3 to 20 cm for typical relative humidities between 1.5 and 90%. The wet delay is therefore more variable but at least 10 times smaller than the dry delay at the MeerKAT site, and it is further alleviated by the fact that the site is never hot and humid, as can be seen in Figure 1.

1.1.2 Excess path length as a function of zenith angle

The excess path length along zenith angle z is $L \approx L_0 \sec z$ for a plane-parallel atmosphere and a flat Earth, which invokes the well-known secant expression for air mass. A more accurate expression that also takes into account the curvature of the Earth with radius $r_0 = 6370$ km is

$$L = L_0 \sec z \left(1 - \frac{h_0}{r_0} \tan^2 z \right) \quad (8)$$

for an exponentially distributed radially symmetric atmosphere with scale height h_0 . Compare this to the corresponding approximation for the refraction angle, $R \approx A \tan z + B \tan^3 z$, which in effect adds an extra $\sin z$ term.

An even more accurate description of air mass is provided by mapping functions in the form of continued fractions [5, 7, 8, 3], analogous to the generator functions used to model refractive bending. In Niell's version [7] the excess path length becomes

$$L = \frac{DL_0}{\cos z + \frac{A}{\cos z + \frac{B}{\cos z + C}}}, \quad (9)$$

where the coefficients A , B and C are optimised to fit L to ray-traces of radiosonde data and standard atmospheric models, and D normalizes the air mass at zenith. Compare this with the first-order model $L = L_0 / \cos z$. Niell's coefficients depend on the day of the year and the receptor latitude and altitude, thereby incorporating seasonal and global deviations from a simple spherical model of air mass. For example, at the MeerKAT site the maximum dry excess path length of 7.8 m at 15° elevation has an annual variation of about 2.5 mm. Wet and dry delays generally have separate mapping functions with different coefficient values, although more advanced models [9] couple the two parts.

The various descriptions of air mass are compared in Figure 2. The air mass increases from 1 at zenith to 3.8 at MeerKAT's elevation limit of 15° . At lower elevations it rapidly increases towards $\sqrt{(\pi r_0)/(2h_0)}$ at the horizon, which is about 35 in the dry case and 70 in the wet case. The basic secant approximation and the spherical approximation of Eq. (8) break down in this region, while Niell's mapping functions remain useful down to 3° elevation.

1.1.3 Differential refraction in an interferometer

An interferometer is sensitive to differential delays between its receptors and not to absolute delay. Two receptors that are close together will experience the same atmospheric conditions and will also have very similar zenith angles (identical in the plane-parallel flat Earth approximation), so that their tropospheric delays cancel out. Interferometers therefore only experience differential refraction. The maximum difference in zenith angle, B/r_0 , is proportional to the baseline length B and is achieved when the source's azimuth angle coincides with the baseline's azimuth angle. For MeerKAT's longest baseline of 8 km this is about 4 arcminutes. For MeerKAT+ it increases to $11'$ and the maximum differential dry excess path length at 15° is only 8.7 cm—about 1% of the corresponding excess path length. As shown

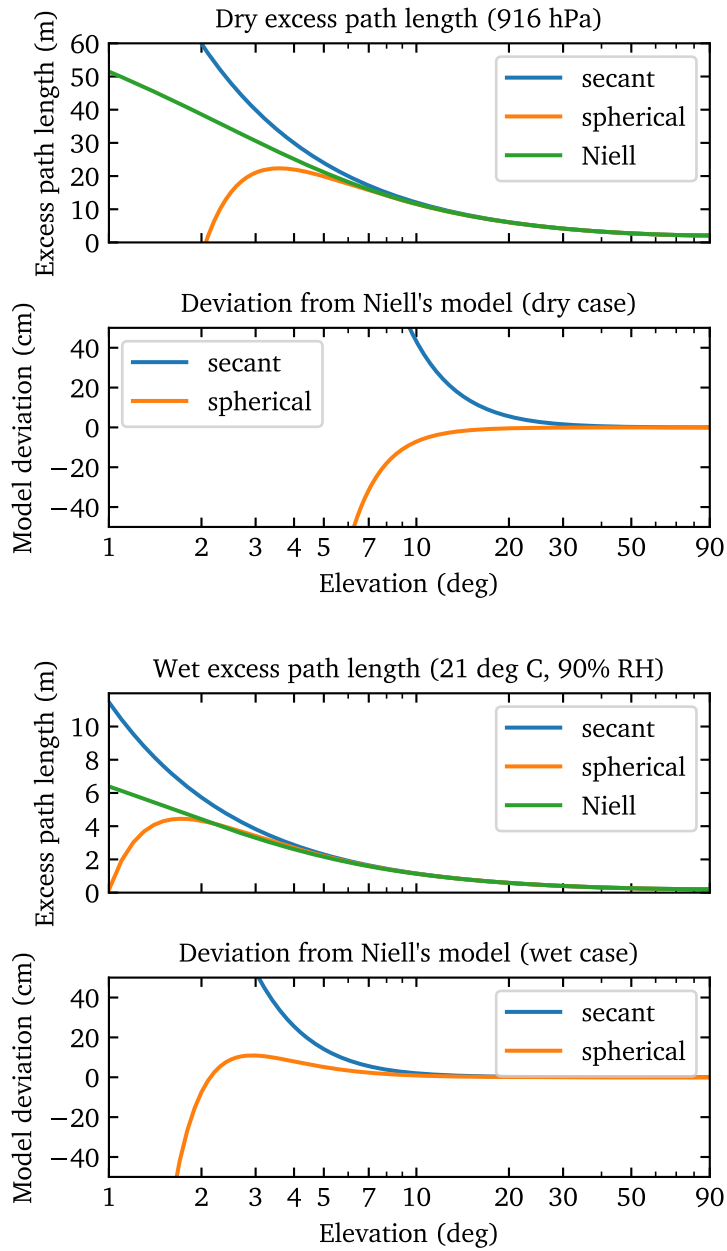


Figure 2: Comparison of various models of excess path length as a function of elevation angle, for both the dry and wet case. The excess path length in the zenith direction (90°) is chosen to be the maximum for the MeerKAT site in 2019. This compares the basic secant model and the spherical model of Eq. (8) to Niell's mapping function of Eq. (9), which is considered to be close to the ideal raytracing model above 3° . The plots for the dry case are equivalent to plots (b) and (c) in Figure 13.6 of [2].

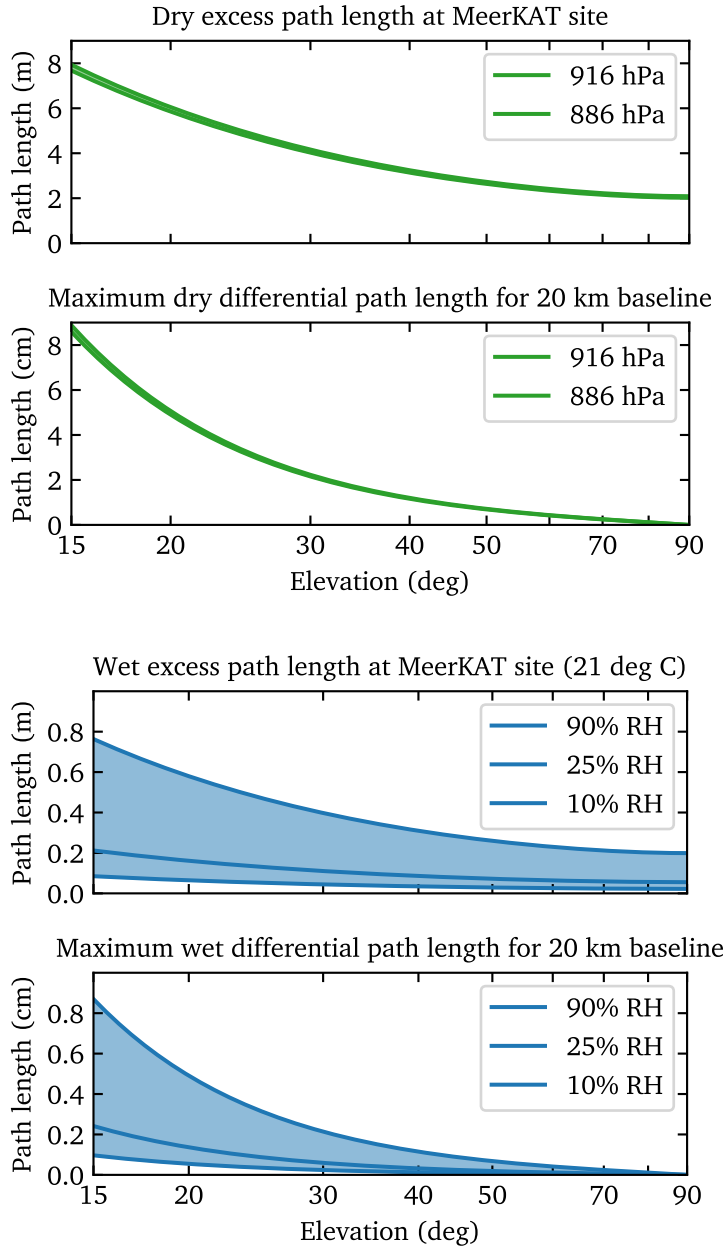


Figure 3: The range of differential path lengths due to tropospheric refraction as experienced by the longest 20-km baseline of MeerKAT+ at various elevation angles, based on typical weather data for the MeerKAT site and a source at an azimuth along the baseline. The dry path length is shown as a function of atmospheric pressure in hPa while the wet path length is shown as a function of relative humidity (RH) for a fixed temperature of 21°C.

in Figure 3, the differential delay also tends to zero at zenith for a connected interferometer since it is related to the gradient of air mass.

The maximum differential path length for a MeerKAT+ baseline of length B km at the elevation limit of 15° is approximately

$$\Delta L_{\text{MAX}} \approx 4.9 \times 10^{-4}(P + H)B + 0.87\Delta P + 0.85\Delta H + 1.1\Delta T \text{ [cm]}, \quad (10)$$

where P is the atmospheric pressure in hPa and H is the relative humidity as a percentage. This is valid around the median operating point of 21°C and relative humidity of 23%. It also includes the effect of changes in the atmosphere between the two receptors: the receptor furthest from the source has ΔP hPa higher pressure and ΔH % higher relative humidity and is ΔT °C warmer than the receptor that is closer. The sensitivities to P , H and T are quite similar; 1 hPa, 1% relative humidity and 1°C all add about 1 cm to the differential path. Baselines longer than 2 km may have path lengths that differ by more than 1 cm.

1.2 Ionospheric delay

The ionosphere differs in several important respects from the atmospheric layers below it⁴. It is a plasma with effects that are strongly frequency dependent (i.e. dispersive) and largely determined by its electron content. The electron content is expressed as the electron density n_e in electrons per cubic metre, or more conveniently as the *total electron content (TEC)*

$$Q = 10^{-16} \int n_e(h) dh \text{ [TECU]}, \quad (11)$$

which integrates the electron density along a ray path through the ionospheric layer and is specified in TEC units⁵ (TECU) of 10^{16} electrons per square metre. The mean TEC is 10 TECU but it can vary from 1 to 100 TECU based on the time of day, season, solar activity and latitude.

The index of refraction of a plasma is less than unity and the phase velocity c/n is greater than the velocity in a vacuum, c . A monochromatic electromagnetic wave therefore experiences a *negative* phase delay, or advance, while travelling through the plasma⁶. The excess path length in the zenith direction is

$$L_0 \approx -\frac{0.403}{\nu^2} Q \text{ [m]} \quad (12)$$

for TEC Q in TEC units and the frequency ν of the incident wave in GHz, based on a parabolic electron density distribution within the ionosphere and $\nu \gg 12$ MHz

⁴This follows the derivation in Chapter 14 of [2], referencing equations (14.14), (14.19) and (14.20), with input from [1].

⁵TEC is equivalent to the dispersion measure (DM) of pulsar astronomy, since both are measurements of electron column density. TEC counts electrons in the ionosphere, while DM counts electrons in the interstellar medium. The common DM unit of 1 pc cm^{-3} is 3,085,678 TECU. For example, the Vela pulsar has a DM of 68 pc cm^{-3} , or 2.1×10^8 TECU. The ionosphere has a much higher electron density (10^6 vs $0.03 \text{ electrons cm}^{-3}$) but is only 200 km thick, so the interstellar column density ends up being much larger due to the vast distances involved.

⁶The group velocity nc is less than c and the group delay is therefore positive. This is the delay experienced by pulses of radiation from e.g. pulsars, resulting in the usual dispersion effect with lower frequencies delayed more than higher frequencies, opposite to the effect on monochromatic waves.

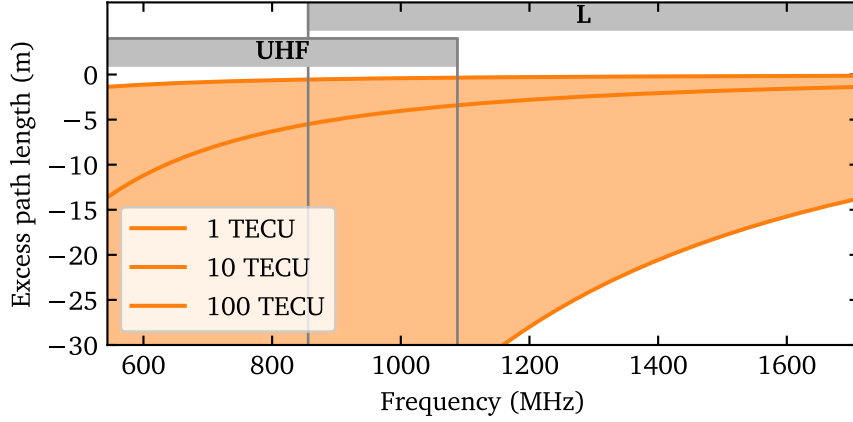


Figure 4: Excess path length in the zenith direction due to the ionosphere, for the MeerKAT UHF and L bands and various TEC values.

(the plasma frequency). L_0 differs from the tropospheric version in Eq. (4) in two important respects: the negative sign and the ν^{-2} dependence. Figure 4 plots L_0 in the MeerKAT UHF and L bands.

Another major difference from the troposphere is that the ionosphere is not close to the Earth's surface. Most of its electrons are concentrated in a relatively thin shell at a height of $h_i \approx 350$ km. Because of this, ionospheric effects do not vary as strongly with zenith angle as in the troposphere. The excess path length L varies approximately as the secant of the zenith angle z_i of the ray as it exits the shell, related to the zenith angle at the observer, z , by

$$z_i = \sin^{-1} \left[\frac{r_0}{r_0 + h_i} \sin z \right], \quad (13)$$

so that

$$L \approx L_0 \sec z_i \approx \frac{L_0}{\sqrt{1 - 0.9 \sin^2 z}}. \quad (14)$$

This is also known as the relation between slant TEC and zenith TEC in the ionospheric science community.

As with tropospheric delays, an interferometer only senses differential ionospheric refraction. In the case of irregular refraction and travelling disturbances this is due to different ionospheric conditions above each receptor. Even if the total electron content is the same for both receptors, they have different zenith angles due to the curvature of the Earth and therefore the visibilities measured on that baseline will exhibit a systematic differential component. This is illustrated for MeerKAT+ in Figure 5.

The maximum differential path length for a MeerKAT+ baseline of length B km at the elevation limit of 15° is approximately

$$\Delta L_i \approx -0.022 Q \nu^{-2} B - 100 \Delta Q \nu^{-2} \text{ [cm]}, \quad (15)$$

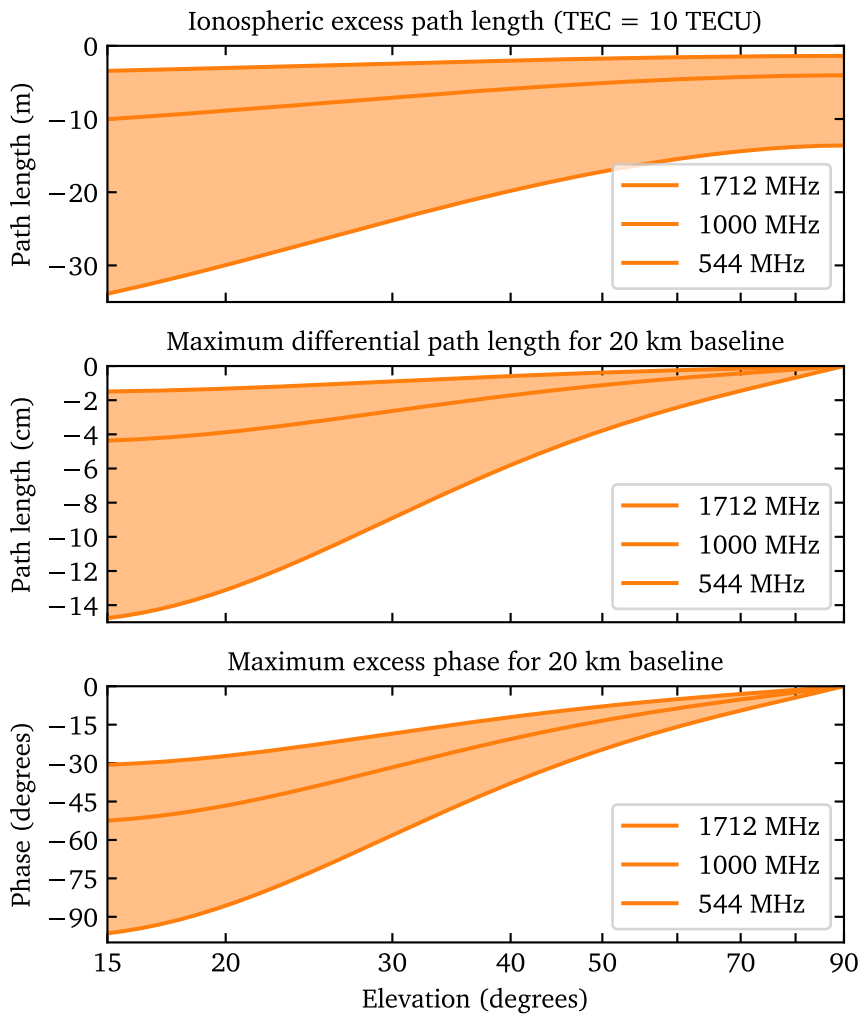


Figure 5: The range of differential path lengths due to systematic ionospheric refraction as experienced by the longest 20-km baseline of MeerKAT+ at various elevation angles and frequencies. The top plot shows the excess path length experienced by a single receptor for an average TEC value, based on Eq. (14). The middle plot shows the differential path length between two receptors spaced 20 km apart, with the source at an azimuth along the baseline. The bottom plot shows the corresponding excess phase.

where Q is the total electron content in TECU and ν is the frequency in GHz. The receptor furthest from the source has ΔQ TECU higher TEC than the receptor that is closer.

The frequency dependency of ionospheric refraction makes it harder to correct in a wideband correlator such as the one in the MeerKAT telescope. Its phase response does not have the constant slope of a pure delay but varies inversely with frequency, which is ideally removed by dedispersion. The differential path length of Eq. (15) is better expressed as the excess phase

$$\Delta\phi_i \approx -0.26Q\nu^{-1}B - 1200\Delta Q\nu^{-1} \text{ [degrees]}. \quad (16)$$

The MeerKAT UHF and L-band receivers have octave bands, which makes the phase difference across the band half of this.

Another challenge for ionospheric correction is the need for accurate TEC measurements. This is somewhat mitigated by generally depressed TEC values during the current solar minimum in 2020, and MeerKAT's requirements that only guarantee precision observations at night.

2 Algorithms and libraries

2.1 CALC

CALC is widely used in the VLBI community to predict delays to high precision. A modified version of CALC 11 is included with the DiFX software correlator [10]. It has also been adopted as a correlator delay model by some connected radio telescopes such as ALMA. It models many geometric effects, conveniently split into three groups, with the relevant Fortran subroutines in square brackets:

1. Basic source / receptor positions and motions [PEP]:
 - The ITRF and ICRF frames and motions within them
 - Time scales (UTC, TAI, TT, UT1, TDB)
 - The Solar System ephemeris (CALC uses JPL's DE421 version)
2. Basic Earth orientation:
 - Precession / nutation [NUTG] (CALC uses the IAU2006 model)
 - Correction to basic Earth orientation parameters (UT1, polar motion) via e.g. IERS bulletins (CALC allows for this manually)
3. More advanced Earth models:
 - Diurnal spin [DIRNL], diurnal polar motion / wobble [WOBG]
 - Earth tides [ETDG], solid-earth pole tides [PTDG]
 - Ocean loading [OCEG], ocean pole tide loading [OPTLG] (both disabled for ALMA)

CALC estimates tropospheric delays in the CATMM module (ATMP and ATMC subroutines). It calculates zenith delays with a combination of Saastamoinen’s refractivity formulas [11] and constants from Davis [5]. It includes a correction to Eq. (5) that accounts for changes in gravity as a function of the receptor’s location. The saturation water vapour pressure is calculated by a well-known formula due to Tetens (1930) [12] based on a form introduced by Magnus in 1844 [13], which is simpler than Crane’s formula [6] but still accurate. CALC used to model the zenith angle dependence of tropospheric delays with Niell’s set of mapping functions (NMF) [7] but has replaced it with the improved Global Mapping Function (GMF) [8].

ALMA uses CALC for geometric delays but replaces its tropospheric model with a more advanced one (ATM [14]) that is more suitable for millimetre wavelengths. CALC does not model ionospheric delays.

2.2 Katpoint

The current stable version of katpoint is based on the PyEphem library [15], which wraps the libastro C library that forms part of XEphem [16]. PyEphem uses older versions of the models in groups 1 and 2 of CALC. The Solar System ephemeris is VSOP87D / DE200 with additional formulas from Jean Meeus’s books [17] and the nutation model is IAU1980. It predates the ICRF (and ITRF) reference frame and uses FK5 instead, and it performs some calculations using single-precision floats. The end result is that PyEphem’s positional accuracy is limited to around 1 arcsecond, which translates to a 4 cm path length difference for MeerKAT on the longest baseline (and 10 cm for MeerKAT+).

PyEphem has an ad hoc time scale where timestamps are treated as TT for Solar System positions but as UTC for Earth orientation purposes. This would allow ad hoc adjustment of UTC timestamps to include UT1 offsets, but katpoint has not used this in its delay model. PyEphem does not use polar motion or fancier Earth models, and also does not calculate any atmospheric delays.

Katpoint uses PyEphem to get the azimuth and elevation of the source at the reference antenna (nominally the array centre). It then turns this into a unit vector in the East-North-Up coordinate system centred on the reference position. The receptor position vectors in this coordinate system are projected onto the unit vector to find the relative offset of each receptor towards the source, which are turned into corresponding delays.

2.3 Astropy

Astropy [18, 19] is a modern Python library that uses the Essential Routines for Fundamental Astronomy (ERFA) library [20] internally. ERFA is in turn derived from the Standards of Fundamental Astronomy (SOFA) library [21], an authoritative set of algorithms endorsed by the IAU. ERFA is functionally equivalent to SOFA but with a less restrictive license.

Like CALC, Astropy supports the ICRF and ITRF frames and various time scales. ERFA provides a simplified Solar System ephemeris but it can also use JPL ephemerides. We use DE421 to match CALC. Astropy also uses the IAU2006 nutation

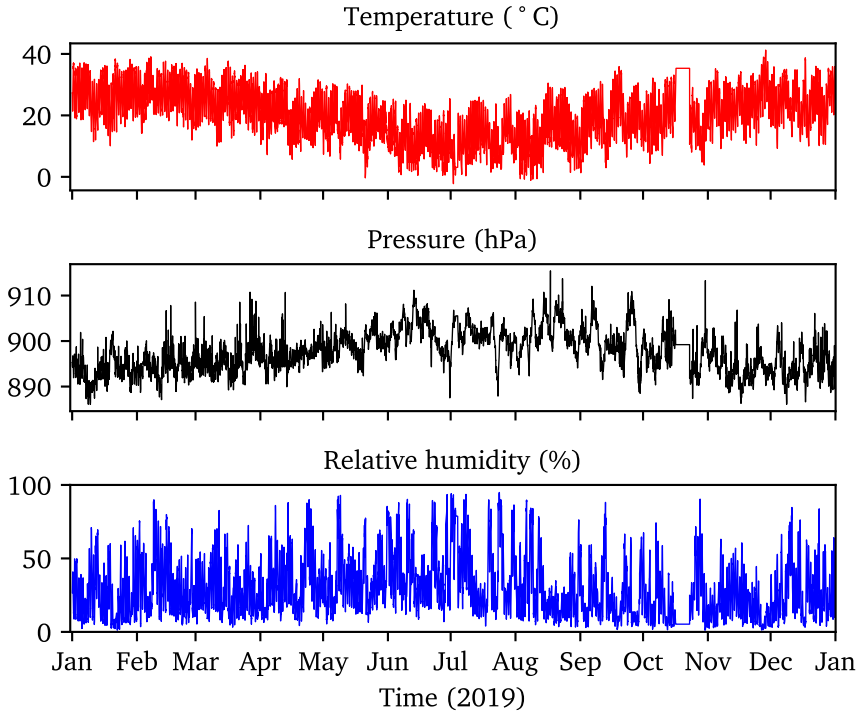


Figure 6: Weather sensor data at the MeerKAT site for 2019.

model by default. It allows automatic UT1 and polar motion correction using IERS bulletins. We load the IERS A bulletin manually so that it can also be provided to CALC. Astropy does not have the fancier Earth models mentioned in group 3 of CALC and also does not model tropospheric or ionospheric delays.

We calculate delays with the centre of the Earth as reference position, by converting an ICRF source position to a Cartesian direction vector in the ITRF frame and then projecting the receptor XYZ coordinate vectors onto that.

3 Benchmarks

We compare the delays produced by katpoint, CALC and Astropy on a year’s worth of observations of the primary calibrator J1939-6342 with ICRF position $RA = 19^h 39^m 25^s 02671$, $Dec. = -63^\circ 42' 45'' 6255$. We track the source above 15° elevation for the 2019 calendar year using the original 64 MeerKAT receptors as well as 20 additional SKA receptors, collectively referred to as MeerKAT+. The longest MeerKAT+ baseline is 17.7 km while the longest MeerKAT baseline is 7.7 km. We use actual temperatures, atmospheric pressures and relative humidities measured at the MeerKAT site in 2019 to model the tropospheric delays, as depicted in Figure 6. Unfortunately we do not have corresponding ionospheric TEC measurements.

Figure 7 shows katpoint and Astropy geometric delays compared to CALC. Since katpoint does not apply UT1 and polar motion corrections, we ran CALC in a similar fashion to get an idea of the intrinsic accuracy of PyEphem. This was on the order of 4 cm on the longest MeerKAT+ baselines, 1.5 cm on the longest existing MeerKAT baselines and below 0.5 cm for the core baselines. This degrades by a factor of 3 once Earth orientation parameters are properly corrected in CALC, indicating the need for this feature in katpoint. Astropy performs an order of magnitude better than this, with path length differences below 1 cm even on the longest MeerKAT+ baselines, and below 1 mm on core baselines.

Figure 8 shows the tropospheric delays predicted by CALC based on the actual MeerKAT weather data of 2019. The delays are differential, with the first receptor (m000) serving as reference. While the worst-case differential path lengths on the longest MeerKAT+ baseline match those in Figure 3, i.e. about 8 cm in the dry case and 0.8 cm in the wet case, the average values are much lower: about 2.2 cm in the dry case and about 0.7 mm in the wet case.

4 Conclusions

Migrating katpoint from PyEphem to Astropy will improve geometric delays by an order of magnitude, compared to the gold standard of CALC. Half of this improvement is due to proper integration of EOP correction via IERS bulletins. While Astropy shares a large part of CALC’s feature set (groups 1 and 2), it is worth looking at the fancier Earth models (group 3) to see if some of them can bring the two libraries even closer together.

We should predict tropospheric delays using the best parts of CALC and Thompson, Moran and Swenson [2]. CALC contains a Fortran implementation of the Global Mapping Function of Boehm [8], which seems to be the most accurate centimetre-wave mapping function that does not rely on dynamically updated weather models. The dry and wet zenith excess path length routines might still be improved by basing it on formulas in [2].

Ionospheric delay is trickier to correct due to the need for accurate TEC values and its curved phase response, which would either require dedispersion in the correlator as part of delay compensation, or correction after correlation, typically during calibration in the SDP pipeline.

References

- [1] R. Hinder and M. Ryle, “Atmospheric limitations to the angular resolution of aperture synthesis radio telescopes,” *Monthly Notices of the Royal Astronomical Society*, vol. 154, no. 2, pp. 229–253, Oct. 1971. [Online]. Available: <https://doi.org/10.1093/mnras/154.2.229>
- [2] A. R. Thompson, J. Moran, and J. George W. Swenson, *Interferometry and Synthesis in Radio Astronomy*, 3rd ed. Springer International Publishing,

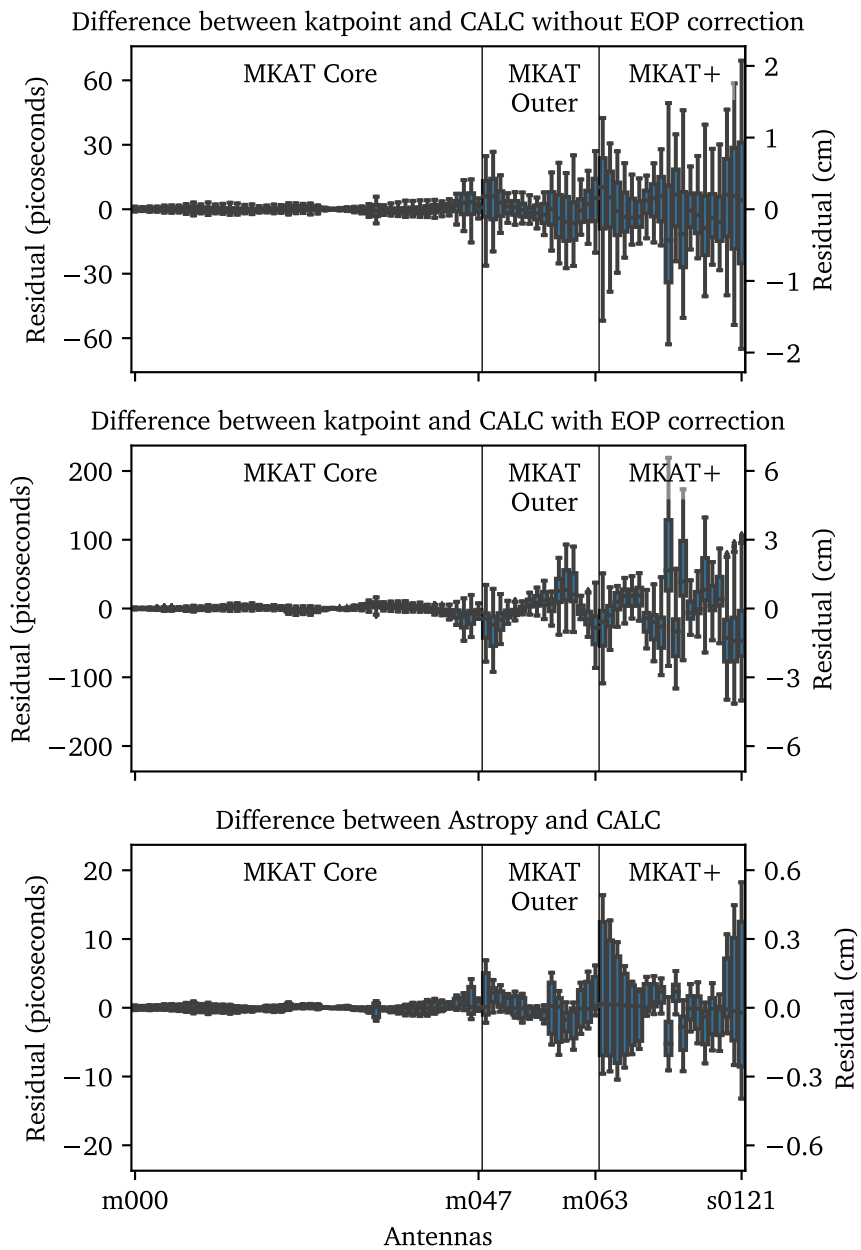


Figure 7: Katpoint and Astropy geometric delays compared to CALC. The delays are calculated over the period of a year while tracking J1939-6342 and the residuals are displayed per receptor (sorted by name, which effectively sorts by baseline length). The top plot used CALC delays without UT1 and polar motion correction from the IERS bulletins to show the intrinsic katpoint accuracy. The middle plot added the CALC corrections back in to show the current practical accuracy for katpoint. The bottom plot shows Astropy's geometric delays versus CALC. Note the different scale on each y-axis.

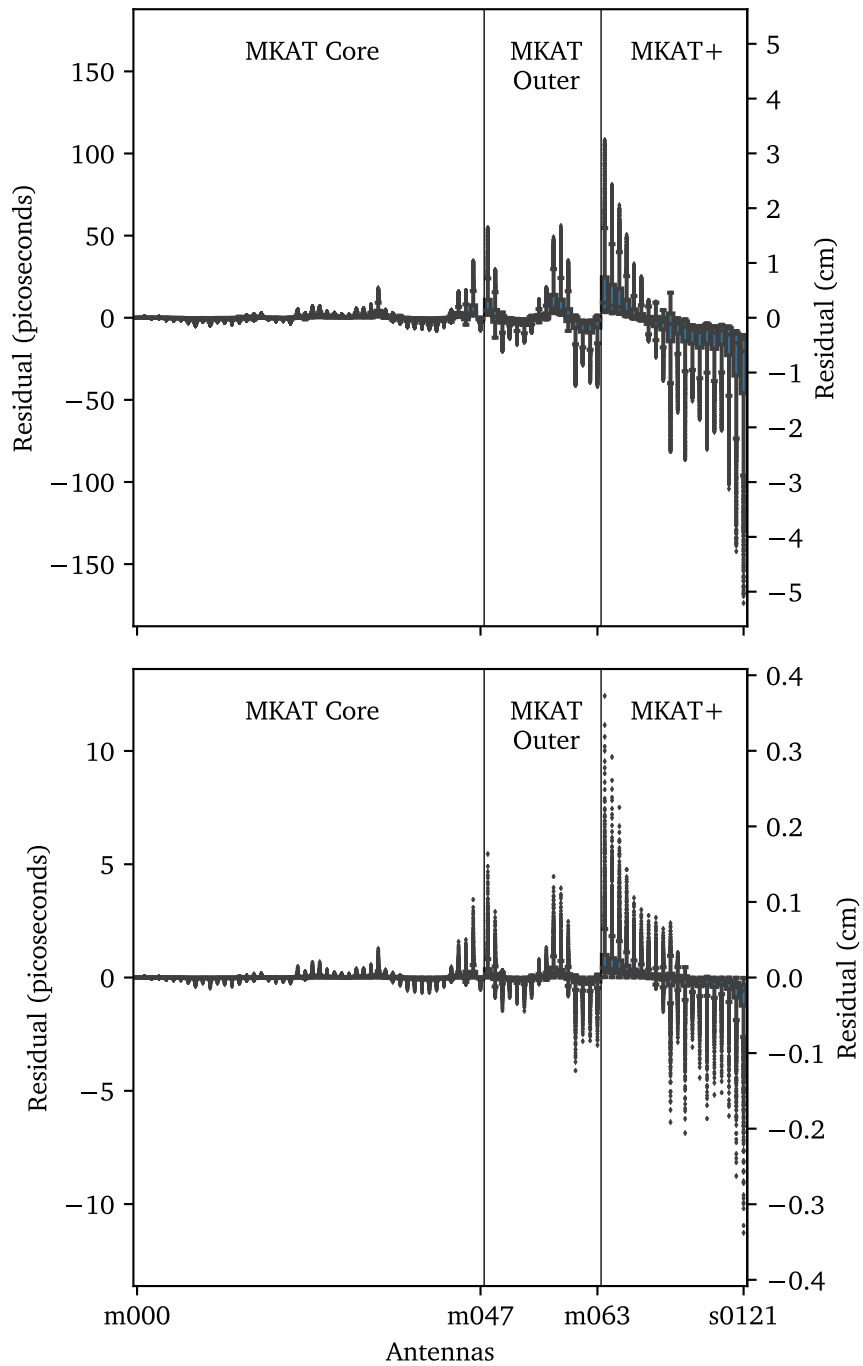


Figure 8: Tropospheric delays predicted by CALC using actual 2019 weather data. The top plot shows the hydrostatic or dry delay, while the bottom plot shows the wet delay. Both are differential delays relative to the first receptor (m000).

2017. ISBN 978-3-319-44431-4. [Online]. Available: <https://doi.org/10.1007/978-3-319-44431-4>
- [3] J. G. Mangum and P. Wallace, "Atmospheric refractive electromagnetic wave bending and propagation delay," *Publications of the Astronomical Society of the Pacific*, vol. 127, no. 947, pp. 74–91, Jan 2015. [Online]. Available: <https://doi.org/10.1086/679582>
- [4] J. Rüeger, "Refractive index formulae for radio waves," in *Proceedings of the FIG XXII International Congress, Washington, D. C.*, Apr 2002. [Online]. Available: https://www.fig.net/resources/proceedings/fig_proceedings/fig_2002/Js28/JS28_rueger.pdf
- [5] J. L. Davis, T. A. Herring, I. I. Shapiro, A. E. E. Rogers, and G. Elgered, "Geodesy by radio interferometry: Effects of atmospheric modeling errors on estimates of baseline length," *Radio Science*, vol. 20, no. 6, pp. 1593—1607, 1985. [Online]. Available: <https://doi.org/10.1029/rs020i006p01593>
- [6] R. K. Crane, "Refraction effects in the neutral atmosphere," in *Astrophysics*, ser. Methods in Experimental Physics, M. Meeks, Ed. Academic Press, 1976, vol. 12, pp. 186–200. [Online]. Available: [https://doi.org/10.1016/S0076-695X\(08\)60686-9](https://doi.org/10.1016/S0076-695X(08)60686-9)
- [7] A. E. Niell, "Global mapping functions for the atmosphere delay at radio wavelengths," *Journal of Geophysical Research: Solid Earth*, vol. 101, no. B2, pp. 3227–3246, Feb 1996. [Online]. Available: <https://doi.org/10.1029/95JB03048>
- [8] J. Boehm, A. Niell, P. Tregoning, and H. Schuh, "Global Mapping Function (GMF): A new empirical mapping function based on numerical weather model data," *Geophysical Research Letters*, vol. 33, no. L07304, Apr 2006. [Online]. Available: <https://doi.org/10.1029/2005GL025546>
- [9] G. E. Lanyi, "Tropospheric delay effects in radio interferometry," Jet Propulsion Laboratory, Pasadena, California, The Telecommunications and Data Acquisition Progress Report 42-78, April-June 1984. [Online]. Available: https://tmo.jpl.nasa.gov/progress_report/42-78/78N.PDF
- [10] D. Gordon, W. Briskin, and W. Max-Moerbeck, "Difxcalc - Calc11 for the DiFX correlator," in *International VLBI Service for Geodesy and Astrometry 2016 General Meeting Proceedings: "New Horizons with VGOS"*, D. Behrend, K. D. Baver, and K. L. Armstrong, Eds., vol. NASA/CP-2016-219016, 2016. [Online]. Available: https://ivscc.gsfc.nasa.gov/publications/gm2016/039_gordon_etal.pdf
- [11] J. Saastamoinen, "Atmospheric correction for the troposphere and stratosphere in radio ranging satellites," in *The Use of Artificial Satellites for Geodesy (Geophysical Monograph Series)*, S. W. Henrikson, A. Mancini, and B. H. Chovitz, Eds., Washington, D.C., 1972, vol. 15, pp. 247–251. ISBN 9781118663646. [Online]. Available: <https://doi.org/10.1029/GM015p0247>
- [12] O. Tetens, "Über einige meteorologische begriffe," *Zeitschrift Geophysic*, vol. 6, pp. 297–309, 1930.

- [13] F. W. Murray, “On the computation of saturation vapor pressure,” *Journal of Applied Meteorology*, vol. 6, no. 1, pp. 203–204, Feb 1967. [Online]. Available: [https://doi.org/10.1175/1520-0450\(1967\)006<0203:OTCOSV>2.0.CO;2](https://doi.org/10.1175/1520-0450(1967)006<0203:OTCOSV>2.0.CO;2)
- [14] J. R. Pardo, J. Cernicharo, and E. Serabyn, “Atmospheric transmission at microwaves (ATM): an improved model for millimeter/submillimeter applications,” *IEEE Transactions on Antennas and Propagation*, vol. 49, no. 12, pp. 1683–1694, Dec 2001. [Online]. Available: <https://doi.org/10.1109/8.982447>
- [15] B. Rhodes, “The pyephem library: v3.7.7.1,” <https://github.com/brandon-rhodes/pyephem>, Feb 2020.
- [16] E. Downey, “The xephem software package: v3.7.7,” <https://www.clearskyinstitute.com/xephem/>, Aug 2015.
- [17] J. Meeus, *Astronomical Algorithms*, 1st ed. Willmann-Bell, Inc., Richmond, Virginia, USA, 1991. ISBN 0943396352
- [18] Astropy Collaboration, T. P. Robitaille, E. J. Tollerud, P. Greenfield, M. Droettboom, E. Bray, T. Aldcroft, M. Davis, A. Ginsburg, A. M. Price-Whelan, W. E. Kerzendorf, A. Conley, N. Crighton, K. Barbary, D. Muna, H. Ferguson, F. Grollier, M. M. Parikh, P. H. Nair, H. M. Unther, C. Deil, J. Woillez, S. Conseil, R. Kramer, J. E. H. Turner, L. Singer, R. Fox, B. A. Weaver, V. Zabalza, Z. I. Edwards, K. Azalee Bostroem, D. J. Burke, A. R. Casey, S. M. Crawford, N. Dencheva, J. Ely, T. Jenness, K. Labrie, P. L. Lim, F. Pierfederici, A. Pontzen, A. Ptak, B. Refsdal, M. Servillat, and O. Streicher, “Astropy: A community Python package for astronomy,” *Astronomy & Astrophysics*, vol. 558, p. A33, Oct. 2013. [Online]. Available: <https://dx.doi.org/10.1051/0004-6361/201322068>
- [19] A. M. Price-Whelan, B. M. Sipőcz, H. M. Günther, P. L. Lim, S. M. Crawford, S. Conseil, D. L. Shupe, M. W. Craig, N. Dencheva, A. Ginsburg, J. T. VanderPlas, L. D. Bradley, D. Pérez-Suárez, M. de Val-Borro, P. Paper Contributors, T. L. Aldcroft, K. L. Cruz, T. P. Robitaille, E. J. Tollerud, A. Coordination Committee, C. Ardelean, T. Babej, Y. P. Bach, M. Bachetti, A. V. Bakanov, S. P. Bamford, G. Barentsen, P. Barmby, A. Baumbach, K. L. Berry, F. Biscani, M. Boquien, K. A. Bostroem, L. G. Bouma, G. B. Brammer, E. M. Bray, H. Breytenbach, H. Buddelmeijer, D. J. Burke, G. Calderone, J. L. Cano Rodríguez, M. Cara, J. V. M. Cardoso, S. Cheedella, Y. Copin, L. Corrales, D. Crichton, D. D’Avella, C. Deil, É. Depagne, J. P. Dietrich, A. Donath, M. Droettboom, N. Earl, T. Erben, S. Fabbro, L. A. Ferreira, T. Finethy, R. T. Fox, L. H. Garrison, S. L. J. Gibbons, D. A. Goldstein, R. Gommers, J. P. Greco, P. Greenfield, A. M. Groener, F. Grollier, A. Hagen, P. Hirst, D. Homeier, A. J. Horton, G. Hosseinzadeh, L. Hu, J. S. Hunkeler, Ž. Ivezić, A. Jain, T. Jenness, G. Kanarek, S. Kendrew, N. S. Kern, W. E. Kerzendorf, A. Khvalko, J. King, D. Kirkby, A. M. Kulkarni, A. Kumar, A. Lee, D. Lenz, S. P. Littlefair, Z. Ma, D. M. Macleod, M. Mastroiello, C. McCully, S. Montagnac, B. M. Morris, M. Mueller, S. J. Mumford, D. Muna, N. A. Murphy, S. Nelson, G. H. Nguyen, J. P. Ninan, M. Nöthe, S. Ogaz, S. Oh, J. K. Parejko, N. Parley, S. Pascual, R. Patil, A. A. Patil, A. L. Plunkett, J. X. Prochaska, T. Rastogi, V. Reddy Janga, J. Sabater, P. Sakurikar, M. Seifert, L. E. Sherbert, H. Sherwood-Taylor, A. Y. Shih, J. Sick, M. T. Silbiger, S. Singanamalla, L. P. Singer, P. H. Sladen, K. A.

- Sooley, S. Sornarajah, O. Streicher, P. Teuben, S. W. Thomas, G. R. Tremblay, J. E. H. Turner, V. Terrón, M. H. van Kerkwijk, A. de la Vega, L. L. Watkins, B. A. Weaver, J. B. Whitmore, J. Woillez, V. Zabalza, and A. Contributors, “The Astropy Project: Building an Open-science Project and Status of the v2.0 Core Package,” *The Astronomical Journal*, vol. 156, p. 123, Sep. 2018. [Online]. Available: <https://doi.org/10.3847/1538-3881/aabc4f>
- [20] E. Tollerud, S. Pascual, P. Nair, J. Woillez, T. Jenness, O. Streicher, and M. Droettboom, “The ERFA library: v1.7.0,” <https://github.com/liberfa/erfa>, Dec. 2019.
- [21] “IAU SOFA Software Collection: Issue 2019-07-22,” <http://www.iausofa.org>, 2019.